

Automatic Dynamic Parallelotope Bundles for Reachability of Nonlinear Dynamical Systems

Edward Kim

A thesis submitted to the faculty of the University of North Carolina at Chapel Hill in partial fulfillment of the requirements for the degree of Master of Science in the Department of Computer Science in the College of Arts and Science.

Chapel Hill
2022

Approved by:

Committee Member 1

Committee Member 2

Committee Member 3

Committee Member 4

Committee Member 5

Committee Member 6

©2022
Edward im
ALL RIGHTS RESERVED

ABSTRACT

Edward Kim: Automatic Dynamic Parallelotope Bundles for Reachability of Nonlinear Dynamical Systems

(Under the direction of Parasara Sridhar Duggirala)

Reachable set computation is an important technique for the verification of safety properties of dynamical systems. In this thesis, we investigate reachable set computation for discrete nonlinear systems based on parallelotope bundles. The crux of the reachability algorithm relies on computing an upper and lower bound on the supremum and infimum respectively of a nonlinear function over a rectangular domain. We cover two ways of computing these bounds: one method utilizing Bernstein polynomials and the other relying on a non-linear optimization tool developed by NASA, Kodiak. We aim to improve the traditional parallelotope-based reachability method by removing the manual step of parallelotope template selection in order to make the procedure fully automatic. Furthermore, we show that adding templates dynamically during computations can improve accuracy. To this end, we investigate two techniques for generating the template directions. The first technique approximates the dynamics as a linear transformation and generates templates using this linear transformation. The second technique uses Principal Component Analysis (PCA) of sample trajectories for generating templates. We have implemented our approach in a Python-based tool called Kaa. The tool is modular and use two types of global optimization solvers, the first using Bernstein polynomials and the second using the aforementioned Kodiak library. Additionally, we leverage the natural parallelism of the reachability algorithm and parallelize the Kaa implementation. Finally, we demonstrate the improved accuracy of our approach on several standard nonlinear benchmark systems, including a high-dimensional COVID19 model proposed by the Indian Supermodel Committee.

ACKNOWLEDGEMENTS

I would like to thank the UNC Computer Science community for supporting my work and providing me a warm community for pursuing this research. In particular, I would like to thank my advisor, Parasara Sridhar Duggirala, for the opportunity to perform research and participate in his group. Bineet Ghosh, Manish Goyal, Abel Karimi, and Meghan Stuart were all great colleagues and I enjoyed my time exchanging ideas, proofreading drafts, and socializing over group lunches. I would also like to thank Stanley Bak for helping me improve the implementation of Kaa and providing valuable feedback during this research. Juan Garcia made a wonderful colleague and an equally wonderful friend. The nights we raided Peabody and Phillips hall was certainly a memorable time. Finally, I would like to thank my parents and my family for their ardent, un-ending support.

TABLE OF CONTENTS

LIST OF TABLES	vii
LIST OF FIGURES	viii
1 Introduction	1
1.1 Related Work	3
2 Preliminaries	4
2.1 Basic Definitions	4
2.2 Parallelotope-based Reachability	7
2.2.1 Parallelotopes	7
2.2.2 Bernstein Polynomials	13
2.2.3 The Static Algorithm	15
3 Dynamic Parallelotope Bundles	22
3.1 Local Linear Approximations	22
3.2 Principal Component Analysis	23
3.3 The Dynamic Algorithm	24
4 Evaluations	27
4.1 Kaa	27
4.2 Benchmarks	29
4.3 COVID19 Supermodel	29
4.4 Comparison of Template Generation Techniques	32
4.4.1 Accuracy of Dynamic Strategies	32
4.4.2 Performance under Increasing Initial Sets	33

4.4.3	Performance against Random Static Templates	33
5	Conclusion	38
	BIBLIOGRAPHY	39

LIST OF TABLES

4.1	Benchmark models and relevant information	32
-----	---	----

LIST OF FIGURES

2.1	Discretized Dynamics of SIR model.....	6
2.2	Plot of the axis-aligned parallelotope of Example 2.2.	9
2.3	Plot of the rotated parallelotope of Example 2.3.	10
2.4	Reachable set computation using manual and static templates.	18
2.5	Discretized Dynamics of Phosphorlay Model.	19
2.6	Projection of Reachable Set of SIR propagated 300 steps in time.	20
2.7	Projection of Reachable Set of the Phosphorlay model propagated 300 steps in time.....	21
3.1	The Automatic, Dynamic Reachability Algorithm.....	25
4.1	Dynamics for the COVID19 Supermodel.	30
4.2	Reachable Sets for India's COVID19 Confirmed Population for the period 06/21/20-10/01/20.....	31
4.3	Effect of varying ratio between the number of PCA and Linear Approx- imation parallelotopes. The Vanderpol (left) and the FitzHugh-Nagumo Neuron (right) phase plots are shown to illustrate differing effects of vary- ing the PCA/LinApp ratio. The initial set for the Vanderpol model is set to $x \in [0, 0.05]$, $y \in [1.95, 2]$, and the initial set Neuron model is set to $x \in [0.9, 1.1]$, $y \in [2.4, 2.6]$	34
4.4	Tables presenting upper bounds on the total reachable set volume by strat- egy. The static directions are retrieved and/or inspired from Sapo models of equal dimension for benchmarking. The best performing strategy is highlighted in bold.....	35
4.5	Comparison between the performance of diagonal static parallelotope bundles and that of the best performing dynamic parallelotope bundles as the volume of the initial set grows.	36
4.6	Comparison between random static strategies and the best performing dy- namic strategies as the volume of the initial set grows. The total reachable set volumes for random static strategies are averaged over ten trials for each system.	37

CHAPTER 1

Introduction

One of the most widely-used techniques for performing safety analysis of non-linear dynamical systems is reachable set computation. For example, reachability analysis has found many applications in formally verifying the safety properties of Cyber-physical Systems, such as autonomous vehicles (Althoff, 2010), F-16 aircraft (Heidlauf et al., 2018), and those governed by Neural Network Controllers (Tran et al., 2019; Fan et al., 2020; Bak, 2021). The reachable set is defined to be the set of states visited by at least one of the trajectories of the system starting from an initial set and propagated forward in time by a finite fixed number of steps. Computing the exact reachable set for non-linear systems is challenging due to several reasons: First, unlike linear dynamical systems whose solutions can be expressed as closed form, non-linear dynamical systems generally do not admit such a nice form. Second, computationally speaking, current tools for performing non-linear reachability analysis are not very scalable. This is also in stark contrast to several scalable approaches developed for linear dynamical systems (Duggirala and Viswanathan, 2016; Bak and Duggirala, 2017). Finally, computing the reachable set using various set representations involves wrapping error which may be too conservative for practical use. That is, the overapproximation acquired at a given step would increase the conservativeness of the overapproximation for all future steps.

One of the several techniques for computing the overapproximation of reachable sets for discrete non-linear systems is to encode the reachable set through parallelotope bundles. Here, the reachable set is represented as a parallelotope bundle, a geometric data structure representing an intersection of several simpler objects called parallelotopes. One of the advantages of this technique is its exploitation of a special form of non-linear optimization problem to overapproximate the reachable set. The usage of a specific form of non-linear optimization mitigates many drawbacks involved with the scalability of non-linear analysis.

However, wrapping error still remains to be a problem for reachability using parallelotope bundles. An immediate reason stems from the responsibility of the practitioner to define the template directions specifying the parallelotopes. Often, these template directions are selected to be either the cardinal axis directions or some directions from octahedral domains. However, it is not certain that the axis-aligned and octagonal directions are optimal for computing reachable sets over general non-linear dynamics. Additionally, even an expert user of reachable set computation tools may not be able to ascertain a suitable set of template directions for computing reasonably accurate over-approximations of the reachable set. Picking unsuitable template directions would only cause the wrapping error to grow, leading to the aforementioned issue of overly conservative reachable sets.

In this thesis, we investigate techniques for generating template directions automatically and dynamically, which is the culmination of several publications in different venues (Kim and Duggirala, 2020; Kim et al., 2021; Geretti et al., 2021). Specifically, we propose a method where instead of the user providing the template directions to define the parallelotope bundle, he or she specifies the number of templates whose template directions are to be generated by our algorithm automatically.

To this end, we study two techniques for generating the said template directions. First, we compute a local linear approximation of the non-linear dynamics and use the linear approximation to compute the template directions. Second, we generate a set of trajectories sampled from within the reachable set and use Principal Component Analysis (PCA) over these trajectories. We observe that the accuracy of the reachable set can be drastically improved by using templates generated using these two techniques. To address scalability, we demonstrate that even when the size of the initial set increases, our template generation algorithm returns more accurate reachable sets than both manually-specified and random template directions. Finally, we experiment with our dynamic template generation algorithm's effectiveness on approximating the reachable set of high-dimensional COVID19 dynamics proposed by the Indian Supermodel Committee (National Supermodel Committee, 2020). The results were published in an ACM blogpost detailing the utility of reachable set computation in modeling disease dynamics (Bak et al., 2021b).

1.1 Related Work

Reachable set computation of non-linear systems using template polyhedra and Bernstein polynomials has been first proposed in (Dang and Salinas, 2009). In (Dang and Salinas, 2009), Bernstein polynomial representation is used to compute an upper bound of a special type of non-linear optimization problem. This enclosing property of Bernstein polynomials has been actively studied in the area of global optimization (Nataray and Kotecha, 2002; Garloff, 2003; Nataraj and Arounassalame, 2007). Furthermore, several heuristics have been proposed for improving the computational performance of optimization using Bernstein polynomials (Smith, 2009; Muñoz and Narkawicz, 2013).

Several improvements to this algorithm were suggested in (Dang and Testylier, 2012; Sassi et al., 2012) and (Dang et al., 2014) extends it for performing parameter synthesis. The representation of parallelotope bundles for reachability was proposed in (Dreossi et al., 2016) and the effectiveness of using bundles for reachability was demonstrated in (Dreossi, 2017; Dreossi et al., 2017). However, all of these papers used static template directions for computing the reachable set. In other words, the user must specify the template directions before the reachable set computation proceeds.

Using template directions for reachable set has been proposed in (Sankaranarayanan et al., 2008) and later improved in (Dang and Gawlitza, 2011). Leveraging the principal component analysis of sample trajectories for computing reachable set has been proposed in (Stursberg and Krogh, 2003; Chen and Ábrahám, 2011; Seladji, 2017). More recently, connections between optimal template directions for reachability of linear dynamical systems and bilinear programming have been highlighted in (Gronski et al., 2019). For static template directions, octahedral domain directions (Clarisó and Cortadella, 2004) remain a popular choice.

CHAPTER 2

Preliminaries

We begin with some basic definitions pertaining to reachability and parallelotopes. The definition of Bernstein polynomials and their enclosure properties will be stated. Finally, an outline of the reachability algorithm given by (Dreossi et al., 2016) for polynomial dynamical systems will be presented.

2.1 Basic Definitions

As stated in the previous section, this thesis pertains to the reachability analysis of dynamical systems. Roughly speaking, a dynamical system describes the behavior of states in space which is governed by a set of differential equations. The states of the system evolve according to the flow of time and the vector field induced by the governing differential equations.

Towards introducing more terminology, the *state* of a system, denoted as x , lies in a domain $D \subseteq \mathbb{R}^n$ where the solutions to the differential equations are defined. In the reachability analysis literature, there are several definitions for dynamical systems which appear depending on the authors' taste of formalizations. Here is a more rigorous definition appearing in (Dang and Maler, 1998):

Definition 2.1. A *continuous dynamical system* is a tuple $\langle X, f \rangle$ where $X = \mathbb{R}^n$ is finite-dimensional Euclidean space and f is a continuous function on X . A point (state) of $x_0 \in X$ evolves according to a trajectory $\xi(t) : \mathbb{R}^+ \rightarrow X$ such that the following hold:

$$\begin{aligned} \xi(0) &= x_0 \\ \frac{d\xi(t)}{dt} &= f(\xi(t)) \quad \forall t \in \mathbb{R}^+ \end{aligned} \tag{2.1}$$

◇

Note that, by a simple separation of variables argument and an initial value of $\xi(0) = x_0$, Equation 2.1 yields the following form for ξ :

$$\xi(t) = x_0 + \int_0^t f(\xi(\tau))d\tau \quad (2.2)$$

However, many members of the research community choose to simply express the system as:

$$x' = f(x) \quad (2.3)$$

for a continuous function $f : \mathbb{R}^n \rightarrow \mathbb{R}^n$. We restrict our attention to a discretized version of this definition for this thesis:

Definition 2.2. A *discrete-time dynamical system* is denoted as

$$x^+ = f(x) \quad (2.4)$$

where $f : \mathbb{R}^n \rightarrow \mathbb{R}^n$ is a function and x^+ denotes the evolved output state. \diamond

In other words, the function f takes input a state of the system and outputs the next step of the system evolved according to the dynamics. Intuitively speaking, the function f generally represents a discretized version of some specified continuous dynamical system. Here, a discrete-time dynamical system is considered *linear* if its dynamics can be expressed as

$$x^+ = Ax, \quad A \in \mathbb{R}^{n \times n}$$

Otherwise, we deem the system to be *non-linear*. Hence, in particular, a non-linear function f cannot be expressed as some matrix $A \in \mathbb{R}^{n \times n}$.

Examples of prominent non-linear dynamical systems include the Lotka-Volterra predator-prey model (Wangersky, 1978), the Fitz-Hugh Neuron model (FitzHugh, 1961), and the recently introduced COVID19 disease model (National Supermodel Committee , 2020). Throughout this thesis, we discretize any continuous dynamics through the well-known Euler method. Thus, up to some error term of bounded degree, we can turn any non-linear system into the form given by Equation 2.4.

Example 2.1. The SIR Epidemic model is a 3-dimensional dynamical system governed by the following continuous dynamics:

$$\begin{aligned} s' &= \beta \cdot si \\ i' &= \beta \cdot si - \gamma \cdot i \\ r' &= \gamma \cdot i \end{aligned} \tag{2.5}$$

where s, i, r represent the fractions of a population of individuals designated as *susceptible*, *infected*, and *recovered* respectively. There are two parameters, namely β and γ , which influence the evolution of the system. β is labeled as the *contraction rate* and $1/\gamma$ is the *mean infective period*. Discretizing Equation 2.5 according the Euler method yields the dynamics:

$$\begin{aligned} s_{k+1} &= s_k - (\beta \cdot s_k i_k) \cdot \Delta \\ i_{k+1} &= i_k + (\beta \cdot s_k i_k - \gamma \cdot i_k) \cdot \Delta \\ r_{k+1} &= r_k + (\gamma \cdot i_k) \cdot \Delta \end{aligned}$$

Figure 2.1: Discretized Dynamics of SIR model

Here, Δ is the discretization step and the index $k \in \mathbb{N}$ simply represents the current step. Note the non-linear terms $s_k i_k$ which preclude the expression of the dynamics as a linear transformation.

◇

We can now give a discretized version of a trajectory as presented in Definition 2.1. The trajectory of a system that evolves according to Equation 2.4, denoted as ξ_{x_0} , is a sequence x_0, x_1, \dots where $x_{i+1} = f(x_i)$. The k^{th} element in this sequence x_k is denoted as $\xi_{x_0}(k)$.

Definition 2.3. Given an initial set $\Theta \subseteq \mathbb{R}^n$, the *reachable set at step k* , denoted as Θ_k is defined as

$$\Theta_k = \{\xi_x(k) \mid x \in \Theta\} \tag{2.6}$$

If we set the number of steps to be some $n \in \mathbb{N}$, we say the *reachable set* is

$$\Theta = \bigcup_{i=1}^n \Theta_i \quad (2.7)$$

◇

We will see in a future section an example of the reachable set of the discretized SIR model presented in Figure 2.1.

2.2 Parallelotope-based Reachability

2.2.1 Parallelotopes

The heart of our reachability algorithm relies on geometric objects called *parallelotopes*. In this section, we define parallelotopes and two representations for them.

Definition 2.4. A *parallelotope* $P \subset \mathbb{R}^n$ is captured by the tuple $\langle \Lambda, c \rangle$ where $\Lambda \in \mathbb{R}^{2n \times n}$ is a matrix and $c \in \mathbb{R}^{2n}$ is a column vector. We impose the condition that $\Lambda_{i+n} = -\Lambda_i$ for all $i \in \{1, \dots, n\}$ such that

$$x \in P \text{ if and only if } \Lambda x \leq c. \quad (2.8)$$

◇

We deem Λ as the *template direction matrix* where Λ_i denotes the i^{th} row of Λ called the i^{th} *template direction*. The column vector c is called the *offset vector* with $c(i)$ denoting the i^{th} element of c . If we unpack Equation 2.8, we can re-express the inequalities as a conjunction of half-space constraints. If we define $c_u = [c(1), c(2), \dots, c(n)]^T$ and $c_l = [c(n+1), c(n+2), \dots, c(2n)]^T$, then Equation 2.8 tells us that:

$$\Lambda_i x \leq c_u(i) \quad (2.9)$$

$$-\Lambda_i x \leq c_l(i) \quad (2.10)$$

Additionally, the definition of the parallelotope above requires that for each of n “positive” directions, there must exist a corresponding “negative” direction. This is encoded into the template matrix Λ

by the condition $\Lambda_{i+n} = -\Lambda_i$. However, by the observation made above, we only need to keep the positive directions and divide our offset vector into equal components with the top half encoding the offsets for the positive directions and the bottom half encoding the offsets for the negative directions. The bottom half must be multiplied by a negative sign to account for Inequality 2.10. Combining these remarks yields the half-space representation of parallelotope P .

Definition 2.5. The *half-space representation* of parallelotope P is tuple $\langle \Lambda, c_l, c_u \rangle$ where $\Lambda \in \mathbb{R}^{n \times n}$ and $c_l, c_u \in \mathbb{R}^n$ such that

$$P = \{x \mid c_l \leq \Lambda x \leq c_u\} \quad (2.11)$$

◇

In particular, as a bounded intersection of pairs of parallel half-spaces, it is convex.

Example 2.2. Consider the 2D plane, namely \mathbb{R}^2 . We can construct a couple of simple examples of parallelotopes. First, if we define our parallelotope's template direction matrix to be the rows of the matrix:

$$\Lambda = \begin{bmatrix} 1 & 0 \\ 0 & 1 \end{bmatrix} \quad (2.12)$$

We see that our template directions will be the vectors $[1, 0]^T, [0, 1]^T$. Suppose now we set our upper and lower offsets to be:

$$c_l = [1, 1]^T, \quad c_u = [2, 2]^T \quad (2.13)$$

Then by Definition 2.5, the half-space representation is given by:

$$\begin{bmatrix} 1 \\ 1 \end{bmatrix} \leq \begin{bmatrix} 1 & 0 \\ 0 & 1 \end{bmatrix} \begin{bmatrix} x \\ y \end{bmatrix} \leq \begin{bmatrix} 2 \\ 2 \end{bmatrix} \quad (2.14)$$

Accordingly, the bounded region in space will be the intersection of the following linear constraints:

$$\begin{aligned} 1 &\leq x \leq 2 \\ 1 &\leq y \leq 2 \end{aligned} \quad (2.15)$$

This is exactly the shifted unitbox $[1, 2] \times [1, 2]$. In fact, we can easily generalize this a general n -dimensional system by considering the template direction matrix $\Lambda = I_n$ where I_n is the $n \times n$

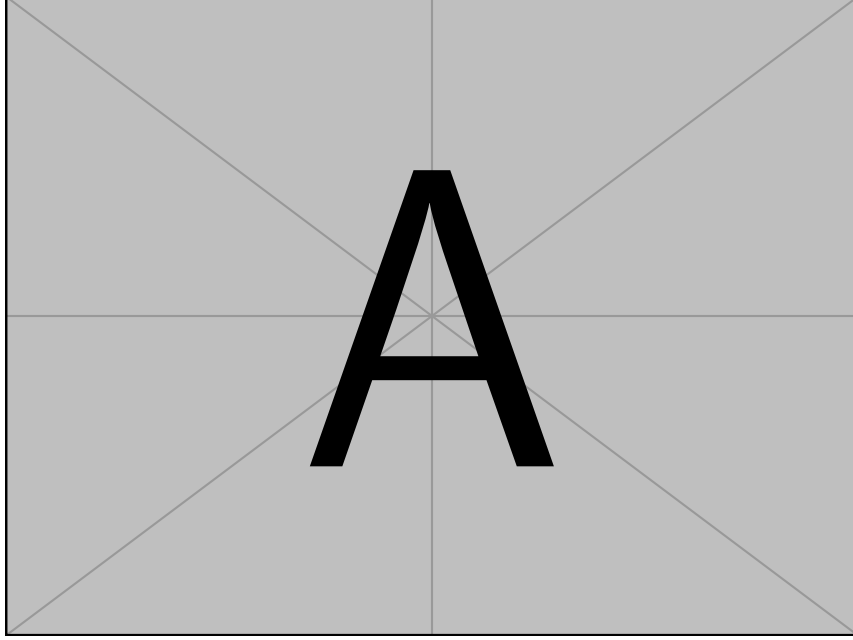


Figure 2.2: Plot of the axis-aligned parallelotope of Example 2.2.

identity matrix and two offset vectors c_l, c_u of length n . This would yield the shifted n -dimensional unitbox:

$$[c_l(1), c_u(1)] \times [c_l(2), c_u(2)] \times \cdots \times [c_l(n), c_u(n)] \quad (2.16)$$

It is worth noting that axis-aligned box on the 2D plane above would give the representation:

$$\Lambda = \begin{bmatrix} 1 & 0 \\ 0 & 1 \\ -1 & 0 \\ 0 & -1 \end{bmatrix}, \quad c = [2, 2, -1, -1]^T \quad (2.17)$$

if we were to convert the half-space representation above into the form defined in Equation 2.8. From here on out, we refer to parallelotopes defined by the n axis-aligned directions as the *axis-aligned* parallelotopes. For a visual plot of above axis-aligned parallelotope, see Figure 2.2

◇

Example 2.3. We can also consider the axis-aligned directions rotated 45° counter-clockwise. This would yield the two diagonal directions $[1, 1]^T, [-1, 1]^T$. Suppose we set the upper and lower offsets

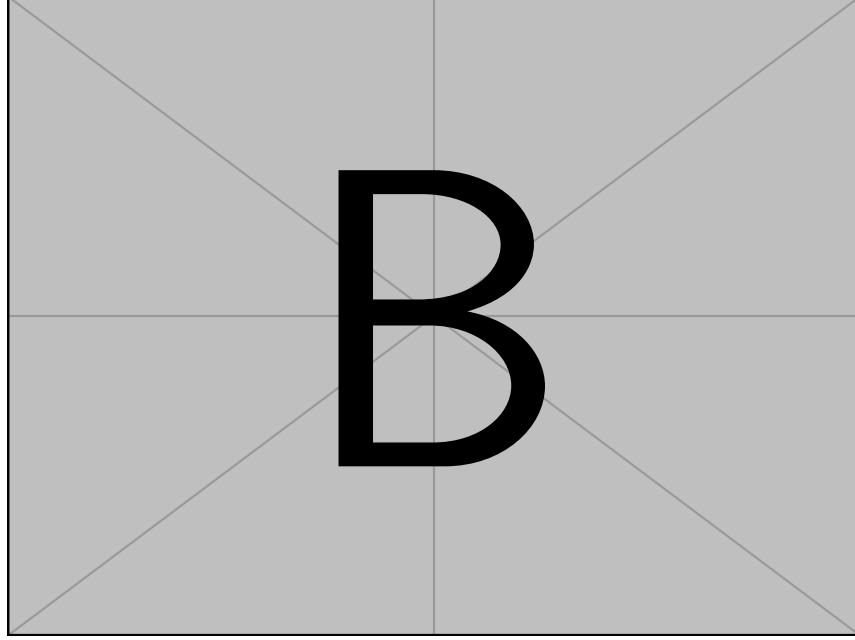


Figure 2.3: Plot of the rotated paralleloptope of Example 2.3.

to be $c_u = [1, 1]^T$ and $c_l = [-1, -1]^T$ respectively, then once again by Definition 2.5:

$$\begin{bmatrix} -1 \\ -1 \end{bmatrix} \leq \begin{bmatrix} 1 & 1 \\ -1 & 1 \end{bmatrix} \begin{bmatrix} x \\ y \end{bmatrix} \leq \begin{bmatrix} 2 \\ 2 \end{bmatrix} \quad (2.18)$$

The bounded region in \mathbb{R}^2 will be the conjunction of the linear inequalities:

$$\begin{aligned} -1 &\leq x + y \leq 1 \\ -1 &\leq y - x \leq 1 \end{aligned} \quad (2.19)$$

In general, we define *diagonal directions* are defined to be vectors created by adding and subtracting distinct pairs of unit axis-aligned vectors from each other. As a matter of convenience however, we refer to *diagonal parallelotopes* as those defined by a combination of axis-aligned and diagonal directions. This definition will be useful when we consider parallelotopes defined by unconventional directions (i.e those template directions which are neither axis-aligned nor diagonal). To see a visual plot of the diagonal paralleloptope, see Figure 2.3.

◇

Alternatively, a paralleloptope can also be represented in a generator representation.

Definition 2.6. The *generator representation* of a parallelotope P is a tuple of vectors $\langle v, g_1, \dots, g_n \rangle$ such that $v, g_1, \dots, g_n \in \mathbb{R}^n$. The vector $v \in \mathbb{R}^n$ is called the *anchor* and the $g_i \in \mathbb{R}^n$, are called the *generators*. The parallelotope is defined as the set:

$$P := \{x \mid \exists \alpha_1, \dots, \alpha_n \in [0, 1], x = v + \sum_{i=1}^n \alpha_i g_i\}$$

◇

This is essentially a convex representation of the parallelotope, which shares many similarities to Zonotopes (Girard, 2005; Althoff et al., 2010) and Star sets (Duggirala and Viswanathan, 2016). In particular, a parallelotope is a special case of a zonotope where the number of generators is exactly the dimension of the system n .

There is a simple method to convert from the half-space representation of P to its equivalent generator representation:

Half-Space to Generator Representation Conversion Procedure

1. Obtain vertex v_1 by solving the linear equation $\Lambda x = c_l$.
2. The $j + 1$ vertex is obtained by solving the linear equation $\Lambda x = \mu_j$ where $\mu_j[i] = c_l[i]$ when $i \neq j$ and $\mu_j[j] = c_u[j]$.
3. The anchor v of the parallelotope is the vertex v_1 and the generators will be $g_i = v_{i+1} - v_1$.

There also exists a procedure to perform the reverse direction, namely to convert from the generator representation to the half-space representation. However, we will not need this procedure for this thesis. Refer to (Dang et al., 2014) for a more detailed exposition of these conversions.

As a final remark, notice that for a parallelotope P , the generator representation also defines an affine transformation that maps $[0, 1]^n$ to P . We refer to this affine transformation associated to P as $T_P : [0, 1]^n \rightarrow P$ when necessary.

Example 2.4. Let us return to the axis-aligned box considered in Example 2.2. To obtain the anchor, we end up with the trivial solution $x = 1, y = 1$ by adhering to Step 1. Hence, the

anchor is set to $v = (1, 1)$. Subsequently, we solve for the two other vertices by following Step 2 to obtain $x = 2, y = 1$ and $x = 1, y = 2$. By Step 3, this would imply that the two generators are $g_1 = (2, 1) - (1, 1) = (1, 0)$ and $g_2 = (1, 2) - (1, 1) = (0, 1)$. Now combine the anchor and generators to get the generator representation for this parallellotope:

$$P = (1, 1) + \alpha_1 \cdot (1, 0) + \alpha_2 \cdot (0, 1) \quad \alpha_1, \alpha_2 \in [0, 1] \quad (2.20)$$

This is exactly the unit box $[0, 1]^2$ with its corner at the origin shifted to $(1, 1)$. \diamond

Example 2.5. Once again, consider the space \mathbb{R}^2 and the parallelotope P given in half-plane representation as $0 \leq x - y \leq 1, 0 \leq y \leq 1$. This is a parallelotope with vertices at $(0, 0)$, $(1, 0)$, $(2, 1)$, and $(1, 1)$. In the half-space representation, the template directions of the parallelotope P are given by the directions $[1, -1]$ and $[0, 1]$. The half-space representation in matrix form is given as follows:

$$\begin{bmatrix} 0 \\ 0 \end{bmatrix} \leq \begin{bmatrix} 1 & -1 \\ 0 & 1 \end{bmatrix} \begin{bmatrix} x \\ y \end{bmatrix} \leq \begin{bmatrix} 1 \\ 1 \end{bmatrix}. \quad (2.21)$$

To compute the generator representation of P , we need to compute the *anchor* and the *generators*. The anchor is obtained by solving the linear equations $x - y = 0, y = 0$. Therefore, the anchor a is the vertex at origin $(0, 0)$. To compute the two generators of the parallelotope, we compute two vertices of the parallelotope. Vertex v_1 is obtained by solving the linear equations $x - y = 1, y = 0$. Therefore, vertex v_1 is the vertex $(1, 0)$. Similarly, vertex v_2 is obtained by solving the linear equations $x - y = 0, y = 1$. Therefore, v_2 is the vertex $(1, 1)$. The generator g_1 is the vector $v_1 - a$, that is $(1, 0) - (0, 0) = (1, 0)$. The generator g_2 is the vector $v_2 - a$, that is $(1, 1) - (0, 0) = (1, 1)$. Therefore, all the points in the parallellotope can be written as $(x, y) = (0, 0) + \alpha_1 \cdot (1, 0) + \alpha_2 \cdot (1, 1)$, $\alpha_1, \alpha_2 \in [0, 1]$. \diamond

Definition 2.7. A parallelotope bundle Q is a set of parallelotopes $\{P_0, \dots, P_m\}$ such that

$$Q = \bigcap_{i=1}^m P_i$$

.

\diamond

Remark 2.1. There is a slight abuse of notation above where we refer to the parallelotope bundle Q as both the set of parallelotopes and the region in \mathbb{R}^n of the intersection of all the parallelotopes P_i . To specify the *set of parallelotopes* which consists the bundle, we will write

$$\mathcal{P}(Q) = \{P_0, \dots, P_m\}$$

This parallelotope bundle will be the geometric data structure which will enclose the region we compute to be the approximation of the exact reachable set. Observe that Q can be expressed as the conjunction of all the linear constraints defining each parallelotope $P_i \in \mathcal{P}(Q)$.

2.2.2 Bernstein Polynomials

In this section, we define Bernstein polynomials and state some of their enclosure properties. A *multi-index* \mathbf{i} of length n is defined as tuple of n elements $\mathbf{i} = (i_1, \dots, i_n)$ such that each $i_k \in \mathbb{N}$. Furthermore, we order the multi-indices as follows: if \mathbf{i} and \mathbf{j} are two multi-indices of length n , then

$$\mathbf{i} \leq \mathbf{j} \iff i_k \leq j_k, \quad 1 \leq k \leq n$$

Finally, we generalize the product of binomial coefficients as:

$$\binom{\mathbf{i}}{\mathbf{j}} := \prod_{k=1}^n \binom{i_k}{j_k}$$

Given two multi-indices \mathbf{i} and \mathbf{d} of size n , where $\mathbf{i} \leq \mathbf{d}$, the Bernstein basis polynomial of degree \mathbf{d} and index \mathbf{i} is defined as:

$$\mathcal{B}_{(\mathbf{i}, \mathbf{d})}(\mathbf{x}) = \beta_{i_1, d_1}(x_1) \beta_{i_2, d_2}(x_2) \dots \beta_{i_n, d_n}(x_n). \quad (2.22)$$

where for $i, d, x \in \mathbb{R}$:

$$\beta_{i, d}(x) = \binom{d}{i} x^i (1-x)^{d-i} \quad (2.23)$$

Let $p : \mathbb{R}^n \rightarrow \mathbb{R}$ be a real polynomial of degree at most \mathbf{d} . We can express p as a linear combination of monomials of degree at most \mathbf{d} :

$$p(\mathbf{x}) = \sum_{\mathbf{i} \leq \mathbf{d}} a_{\mathbf{i}} \cdot \mathbf{x}^{\mathbf{i}}$$

where $\mathbf{x}^{\mathbf{i}}$ represents the monomial $x_1^{i_1} x_2^{i_2} \cdots x_n^{i_n}$. Every such real polynomial p of degree at most \mathbf{d} can be represented as linear combination of Bernstein basis polynomials of degree \mathbf{d} :

$$p(\mathbf{x}) = \sum_{\mathbf{i} \leq \mathbf{d}} b_{\mathbf{i}} \cdot \mathcal{B}_{(\mathbf{i}, \mathbf{d})}(\mathbf{x}) \quad (2.24)$$

where $b_{\mathbf{i}}$ denotes the \mathbf{i}^{th} *Bernstein Coefficient*:

$$b_{\mathbf{i}} = \sum_{\mathbf{j} \leq \mathbf{i}} \frac{\binom{\mathbf{i}}{\mathbf{j}}}{\binom{\mathbf{d}}{\mathbf{j}}} \cdot a_{\mathbf{j}} \quad (2.25)$$

In other words, given a polynomial $p(x_1, \dots, x_n) = \sum_{\mathbf{j} \in J} a_{\mathbf{j}} \mathbf{x}_{\mathbf{j}}$ where J is a set of multi-indices iterating through the degrees found in p with $a_{\mathbf{j}} \in \mathbb{R}$, then $p(x_1, \dots, x_n)$ can be converted into its counterpart under the Bernstein basis, $p(x_1, \dots, x_n) = \sum_{\mathbf{j} \in J} b_{\mathbf{j}} \mathcal{B}_{\mathbf{j}}$ where $b_{\mathbf{j}}$ are the corresponding Bernstein coefficients.

The primary advantage of the Bernstein representation of a polynomial $p(x_1, \dots, x_n)$ is that an upper bound on the supremum and lower bound on the infimum of $p(x_1, \dots, x_n)$ in $[0, 1]^n$ can be computed purely by observing the coefficients of the polynomial in the Bernstein basis. Specifically, the upper and lower bounds of $p(x_1, \dots, x_n)$ over $[0, 1]^n$ are bounded by the Bernstein coefficients. We state this as a property without proof.

Property 2.1. (Enclosure Property) Let $p : \mathbb{R}^n \rightarrow \mathbb{R}$ be a real multivariate polynomial of degree \mathbf{d} , and let $p(\mathbf{x}) = \sum_{\mathbf{i} \leq \mathbf{d}} b_{\mathbf{i}} \cdot \mathcal{B}_{(\mathbf{i}, \mathbf{d})}(\mathbf{x})$ be the Bernstein expansion of p , then

$$\min_{\mathbf{i} \leq \mathbf{d}} \{b_{\mathbf{i}}\} \leq \inf_{x \in [0, 1]^n} p(x) \leq \sup_{x \in [0, 1]^n} p(x) \leq \max_{\mathbf{i} \leq \mathbf{d}} \{b_{\mathbf{i}}\}$$

As mentioned earlier, a parallelotope P can also be represented as an affine transformation T_p from $[0, 1]^n$ to P . Therefore, upper bounds on the supremum of a polynomial function p over P is equivalent to upper bound of $p \circ T_p$ over $[0, 1]^n$. A similar argument follows for the lower bound on the infimum. The crux of the reachability algorithm involves exploiting this property

of Bernstein polynomials to approximate the solution of certain non-linear optimization problem involving polynomial predicates over the unitbox, $[0, 1]^n$. We will cover this algorithm in the upcoming section. For a more rigorous exposition on Bernstein polynomials and Property 2.1, refer to (Garloff, 2003).

2.2.3 The Static Algorithm

We will end with an outline of the static algorithm first investigated in works (Dang and Testylier, 2012; Dreossi et al., 2016). As mentioned in the previous section, the building block of the reachability algorithm relies on approximate solutions to a non-linear optimization problem over the unitbox domain. Consider a non-linear function $h : \mathbb{R}^n \rightarrow \mathbb{R}$. The most general form of this optimization problem can be expressed as:

$$\begin{aligned} \max \quad & h(x) \\ \text{s.t.} \quad & x \in [0, 1]^n. \end{aligned} \tag{2.26}$$

In the static algorithm, the user manually specifies the number of parallelotopes and a set of static directions for each parallelotope. In other words, the user must specify the template matrix Λ and its corresponding offset vector c for each parallelotope $P = \langle \Lambda, c \rangle$ contained in the bundle *before* the computation begins.

We now proceed to formally describe the static algorithm. First, a small remark on the template matrix of the parallelotopes P_i contained in some bundle Q . It is possible that some of the parallelotopes share the same template matrix directions. In other words, for $P_i = \langle \Lambda^{P_i}, c^{P_i} \rangle, P_j = \langle \Lambda^{P_j}, c^{P_j} \rangle$ such that $P_i, P_j \in \mathcal{P}(Q)$, there could exist some k such that $\Lambda_k^{P_i} = \Lambda_k^{P_j}$ as row vectors. Thus, a more compact method of encoding the bundle is by taking the *distinct* template directions as rows of a new template matrix Λ^Q along with its corresponding offset vector c^Q . To distinguish between the distinct parallelotopes contained in the bundle, we add a new matrix called $\mathcal{T}^Q \in \mathbb{N}^{p \times n}$ such that \mathcal{T}_i^Q is a vector of row indices of Λ^Q which specify the template directions defining parallelotope $P_i \in \mathcal{P}(Q)$. The number of rows will thus be the number of distinct parallelotopes contained in the bundle $p = |\mathcal{P}(Q)|$.

Remark 2.2. If none of the parallelotopes $P_i \in \mathcal{P}(Q)$ share common template directions, then Λ^Q will simply be the template direction matrices $\{\Lambda^P\}_{P \in \mathcal{P}(Q)}$ concatenated along their rows. This will generally be the matrix generated by the dynamic algorithm we will outline in a future section.

Example 2.6. ◇

Another input to the algorithm is the initial set, given as a parallelotope P_0 . When the initial set is a box, P_0 will be defined by the axis-aligned template directions.

The output of the algorithm is, for each step k , the set $\bar{\Theta}_k$, which is an overapproximation of the reachable set at step k , $\Theta_k \subseteq \bar{\Theta}_k$. The total overapproximation of the reachable set for a finite number of steps n will be $\Theta = \bigcup_{k=1}^n \Theta_k$. The high-level pseudo-code is written in Algorithm 2.4.

The algorithm simply calls `TransformBundle` for each step, producing a new parallelotope bundle computed from the previous step's bundle. To compute the image of Q , the algorithm computes the upper and lower bounds of $f(x)$ with respect to each template direction Λ_i^Q . Since computing the maximum value of $f(x)$ along each template direction on the Q in one-shot is computationally difficult, the algorithm instead computes the maximum value over each of the constituent parallelotopes and uses the minimum of all these maximum values.

The `TransformBundle` operation works as follows. Consider a parallelotope P in the bundle Q . Given a template direction Λ_i^Q , the maximum value of $\Lambda_i^Q f(x)$ for all $x \in Q$ is less than or equal to the maximum value of $\Lambda_i^P \cdot f(x)$ for all $x \in P$ such that Λ_i^Q is a row in Λ^P . Similar argument holds for the minimum value of $\Lambda_i^Q \cdot f(x)$ for all $x \in Q$. Observe that these inequalities hold by virtue of the fact that $Q \subseteq P$ by definition. To describe this more formally: if $\lambda_i^Q = \{P \in \mathcal{P}(Q) \mid \Lambda_i^Q = \Lambda_k^P \text{ for some } k\}$, then

$$\max_{x \in Q} \Lambda_i^Q \cdot f(x) \leq \min_{P \in \lambda_i^Q} \max_{x \in P} \Lambda_i^P \cdot f(x) \quad (2.27)$$

$$\max_{P \in \lambda_i^Q} \min_{x \in P} \Lambda_i^P \cdot f(x) \leq \min_{x \in Q} \Lambda_i^Q \cdot f(x) \quad (2.28)$$

To compute the upper and lower bounds of each template direction $\Lambda_i f(x)$, for all $x \in P$, we perform the following optimization.

$$\begin{aligned} \max \quad & \Lambda_i^P \cdot f(x) \\ \text{s.t.} \quad & x \in P. \end{aligned} \tag{2.29}$$

Note that $\Lambda_i^P \cdot f(x)$ is a dot product between the row vector Λ_i^P and the component-wise dynamics of $f(x)$. This is similar to the method of computing support functions over convex sets (Boyd et al., 2004).

Given that P is a parallelotope, all the states in P can be expressed as a vector summation of anchor and scaled generators. Let $\langle v, g_1, \dots, g_n \rangle$ be the generator representation of P . The optimization problem given in Equation 2.29 would then transform as follows.

$$\begin{aligned} \max \quad & \Lambda_i^P \cdot f(a + \sum_{i=1}^n \alpha_i g_i) \\ \text{s.t.} \quad & \bar{\alpha} \in [0, 1]^n. \end{aligned} \tag{2.30}$$

Equation 2.30 is a form of $\text{optBox}(\Lambda_i \cdot f)$ over $[0, 1]^n$. One can compute an upper-bound to this non-linear optimization by computing the Bernstein coefficients of $\Lambda_i \cdot f(a + \sum_{i=1}^n \alpha_i g_i)$ and taking the maximum and minimum coefficients as shown in Property 2.1. Similarly, we compute the lower-bound of $\Lambda_i \cdot f(x)$ for all $x \in P$ by computing the upperbound of $-1 \times \Lambda_i \cdot f(x)$.

We iterate this process (i.e., computing the upper and lower bound of $\Lambda_i^Q \cdot f(x)$) for each parallelotope in the bundle Q according to Equation 2.27 and Equation 2.28). Therefore, the tightest upper bound on $\Lambda_i^Q \cdot f(x)$ over Q is the least of the upper bounds computed from each of the parallelotopes. A similar argument holds for lower bounds of $\Lambda_i^Q \cdot f(x)$ over Q . Therefore, the image of the bundle Q will be the bundle Q' where the upper and lower bounds for templates directions are obtained by solving a series of non-linear optimization problems of the form presented in Equation 2.29.

```

Input: Dynamics  $f$ , Initial Parallelotope  $P_0$ , Step Bound  $S$ , Template Dirs  $\Lambda$ , indexes for
parallelotopes  $I$ 
Output: Reachable Set Overapproximation  $\bar{\Theta}_k$  for each step  $k$ 
1  $Q_0 = \{P_0\}$ 
2 for  $k \in [1, 2, \dots, S]$  do
3    $Q_k = \text{TransformBundle}(f, Q_{k-1}, \Lambda)$ 
4    $\bar{\Theta}_k = Q_k$ 
5 end
6 return  $\bar{\Theta}_1 \dots \bar{\Theta}_S$ 
7
8 Proc  $\text{TransformBundle}(f, Q, \Lambda)$  :
9    $Q' \leftarrow \{\}; c_u \leftarrow +\infty; c_l \leftarrow -\infty$ 
10  for each parallelotope  $P$  in  $Q$  do
11     $\langle v, G \rangle \leftarrow \text{generatorRepresentation}(P)$ 
12    for each template direction  $\Lambda_i$  in the template directions  $\Lambda$  do
13       $c'_u[i] \leftarrow \min\{\text{optBox}(\Lambda_i \cdot f), c'_u[i]\}$  (Equation 2.30)
14       $c'_l[i] \leftarrow \max\{-1 \times \text{optBox}(-1 \times \Lambda_i \cdot f), c'_l[i]\}$ 
15    end
16  end
17  Construct parallelotopes  $P'_1, \dots, P'_k$  from  $\Lambda, c'_l, c'_u$  and indexes from  $I$ 
18   $Q' \leftarrow \{P'_1, \dots, P'_k\}$ 
19  return  $Q'$ 

```

Figure 2.4: Reachable set computation using manual and static templates.

Finally, once the loop on step two of Algorithm 2.4 halts at step S , the outputted reachable set will be the computed over-approximations $\bar{\Theta}_1, \dots, \bar{\Theta}_S$. As step four within the loop implies, this is simply the image bundles Q' returned by our `TransformBundle` procedure.

Example 2.7. We return to the SIR model briefly treated in Section 2.1. Figure 2.6 shows the reachable set computed with the static algorithm and plotted using the following parameters:

- The parameters of the model are set to $\beta = 0.34$ and $\gamma = 0.05$. The discretization step is set to $\Delta = 0.1$.
- The parallelotope only has one static parallelotope, namely the initial box. This shows that our template matrix for P is

$$\Lambda^Q = \begin{bmatrix} 1 & 0 & 0 \\ 0 & 1 & 0 \\ 0 & 0 & 1 \end{bmatrix} \quad \mathcal{T}^Q = \begin{bmatrix} 0 & 1 & 2 \end{bmatrix}$$

$$c_l^P = \begin{bmatrix} -0.79 & -0.19 & 0 \end{bmatrix}^T \quad c_u^P = \begin{bmatrix} 0.8 & 0.2 & 0 \end{bmatrix}^T$$

- We set the number of time steps $S = 300$.

There are a few points worth noting here. First, by the discussion leading to Definition 2.5, the initial set would be the box $[0.79, 0.8] \times [0.19, 0.2] \times 0$. This can be interpreted as initializing the model such that 79 – 80% of the population is susceptible (not yet infected) with 19 – 20% of the population is infected. As the simulation is beginning, no percentage of the population has recovered from the disease. Hence, the third parameter r is set to zero. Second, since we only have the axis-aligned parallelotope in our initial bundle, the matrix \mathcal{T}^Q will consist of only one row indicating the axis-aligned directions expressed as distinct rows in Λ^Q . \diamond

Example 2.8. To include an example of a higher-dimensional non-linear system, we introduce the Phosphorale model. The Phosphorale model describes a certain cellular regulatory system. It is captured by seven variables governed by the discretized dynamics stated in Figure 2.8:

$$\begin{aligned} x_{k+1}^1 &= x_k^1 + (-\alpha \cdot x_k^1 + \beta \cdot x_k^3 x_k^4) \cdot \Delta \\ x_{k+1}^2 &= x_k^2 + (\alpha \cdot x_k^1 - x_k^2) \cdot \Delta \\ x_{k+1}^3 &= x_k^3 + (x_k^2 - \beta \cdot x_k^3 x_k^4) \cdot \Delta \\ x_{k+1}^4 &= x_k^4 + (\beta \cdot x_k^5 x_k^6 - \beta \cdot x_k^3 x_k^4) \cdot \Delta \\ x_{k+1}^5 &= x_k^5 + (-\beta \cdot x_k^5 x_k^6 + \beta \cdot x_k^3 x_k^4) \cdot \Delta \\ x_{k+1}^6 &= x_k^6 + (\alpha \cdot x_k^7 - \beta \cdot x_k^5 x_k^6) \cdot \Delta \\ x_{k+1}^7 &= x_k^7 + (-\alpha \cdot x_k^7 + \beta \cdot x_k^5 x_k^6) \cdot \Delta \end{aligned}$$

Figure 2.5: Discretized Dynamics of Phosphorlay Model.

Here, we set the two parameters α, β as $\alpha = 0.5$ and $\beta = 5$. The discretization step is set to $\Delta = 0.01$ and we propagate the reachable set for $S = 300$ time steps. Additionally, the initial box is set to be $[1.00, 1.01]^7 \times [-100, 100]$. Under these parameters, Figure 2.7 depicts the projection of the reachable set on the first three variables x_1, x_2, x_3 . The relevant matrices are defined as:

$$\Lambda^Q = \begin{bmatrix} 1 & 0 & 0 & 0 & 0 & 0 & 0 \\ 0 & 1 & 0 & 0 & 0 & 0 & 0 \\ 0 & 0 & 1 & 0 & 0 & 0 & 0 \\ 0 & 0 & 0 & 1 & 0 & 0 & 0 \\ 0 & 0 & 0 & 0 & 1 & 0 & 0 \\ 0 & 0 & 0 & 0 & 0 & 1 & 0 \\ 0 & 0 & 0 & 0 & 0 & 0 & 1 \\ 0 & 0 & 1 & 1 & 0 & 0 & 0 \end{bmatrix}, \quad \mathcal{T}^Q = \begin{bmatrix} 0 & 1 & 2 & 3 & 4 & 5 & 6 \\ 0 & 1 & 2 & 4 & 5 & 6 & 7 \end{bmatrix} \quad (2.31)$$

\mathcal{T}^Q tells us that the bundle consists of the axis-aligned parallelotope (the first row \mathcal{T}_1^Q) and another diagonal parallelotope (the second row \mathcal{T}_2^Q). \diamond

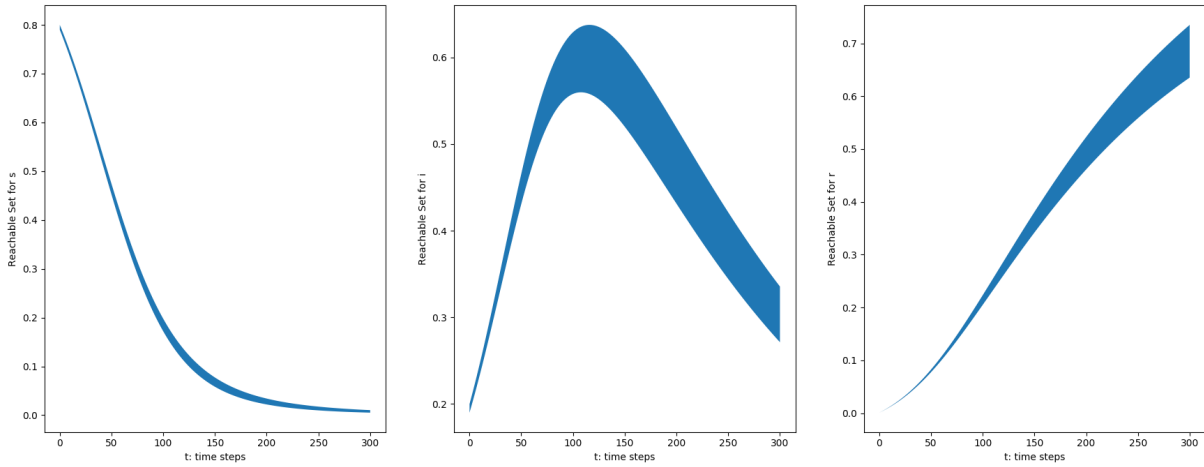


Figure 2.6: Projection of Reachable Set of SIR propagated 300 steps in time.

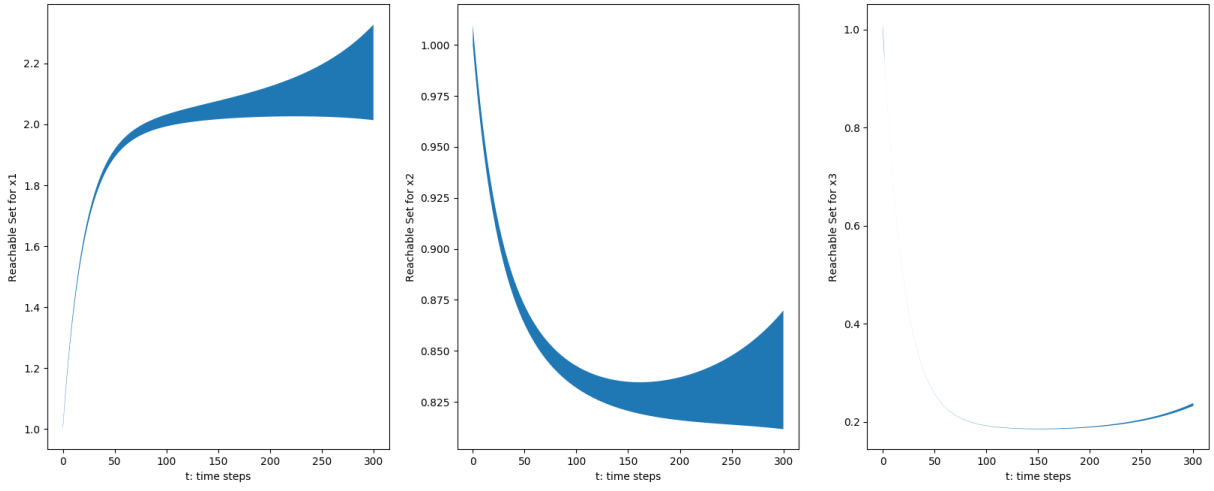


Figure 2.7: Projection of Reachable Set of the Phosporaley model propagated 300 steps in time.

CHAPTER 3

Dynamic Paralleotope Bundles

In this chapter, we cover a method of generating template directions dynamically and automatically. By dynamic, we mean that the template directions must be generated adaptively based on sampled trajectories and/or data from the state of the system. By automatic, we mean that the template directions require no consideration from the user to proceed with the reachable set computation. This is in contrast to the original static algorithm treated in Section 2.2.3 where the user must input his or her own template directions to specify the parallelotopes before the computation starts. To briefly outline the structure of this chapter, we first expound on two techniques we utilize to dynamically generate template directions at each step. The first method is based on local linear approximations where the algorithm approximates the dynamics as a linear transformation based on sample trajectories. The second method is based on Principal Component Analysis (PCA) where the algorithm runs PCA on the end points of the sample trajectories. Finally, we cover the high-level pseudo-code of the dynamic algorithm and explain a set of parameters we feed into the algorithm in order to improve performance and the accuracy of the outputted reachable set.

3.1 Local Linear Approximations

Intuitively speaking, if time step is discretized to be sufficiently small, propagating trajectories according to the non-linear dynamics f for one step could lead to good linear approximations of the dynamics within a small region. To do this, we first sample a set of points in the parallelotope bundle called *support points* and propagate them to the next step using the dynamics f . Support points are a subset of the vertices of the parallelotope that either maximize or minimize the template directions

over the parallelotope bundle. That is the support points are the set of points x_i such that:

$$x_i = \max_{x \in Q} \Lambda_i^Q \cdot x \quad (3.1)$$

for all template directions of the bundle Λ_i^Q . We use the support points as a data-driven approach to find the best-fit linear function to use. These are all found by a straightforward linear program. To find the approximate linear transformation, let x_i denote the support points calculated by Equation 3.1. We perform the following least-squares procedure: the objective would be to find an linear transformation A such that it minimizes the following objective function:

$$\min_A \sum_{x_i} \|f(x_i) - Ax_i\|_2^2 \quad (3.2)$$

where $\|\cdot\|_2$ is the standard 2-norm on \mathbb{R}^n . If the dynamics of a system is linear, i.e., $x^+ = Ax$, the image of the parallelotope $c_l \leq \mathcal{T}x \leq c_u$, is the set $c_l \leq \mathcal{T} \cdot A^{-1}x \leq c_u$. Therefore, given the template directions of the initial set as \mathcal{T}_0 , we compute the local linear approximation of the non-linear dynamics and change the template directions by multiplying them with the inverse of the approximate linear dynamics.

3.2 Principal Component Analysis

The second technique for generating template directions performs Principal Component Analysis (PCA) over the images of the support points. PCA is a standard technique in Statistical Machine Learning used for reduction of dimensionality by performing Singular Value Decomposition (SVD) on the covariance matrix generated by a set of data points. Since the covariance matrix is symmetric (i.e $A = A^T$), the eigenvectors of this matrix will always be a orthonormal basis of the system. Using PCA is a reasonable choice as it produces orthonormal directions that can construct a rotated box for bounding the points.

3.3 The Dynamic Algorithm

Observe that in general, our input dynamics are non-linear and therefore, the reachable set is generally non-convex. On the other hand, a parallelotope bundle is always a convex set. To mitigate the drawbacks of this discrepancy, we can improve accuracy of this representation by considering more template directions and more parallelotopes. To this end, we add a parameter called *template lifespan*, where we use the generated linear approximation and/or PCA template directions not only from the current step but also from previous steps. In our benchmarks, we tune each of the options (PCA / linear approximation as well as lifespan option) to demonstrate that specific parameters generate more accurate reachable sets than those generated by the static algorithm.

The new approach is given in Algorithm 3.1. During each step, the algorithm computes a collection of template directions from the two techniques outlined in Sections 3.1 and 3.2. Each technique will be encoded as a subroutine labeled `ApproxLinearTrans` and `PCA`. The `ApproxLinearTrans` function computes the best approximation of a linear transformation given a list of points before and after the one-step transformation f . The `PCA` function returns a set of orthogonal directions using principal component analysis of a set of points. Now each subroutine will return a collection of n template directions, which in turn will specify exactly one parallelotope. Hence, two parallelotopes, one generated by `ApproxLinearTrans` and the other by `PCA`, can be added to the parallelotope bundle at each step.

There are a few subtle points to be made about the sub-routines used in Algorithm 3.1. First, the algorithm makes use of helper function `hstack`, which attaches two matrices along their rows. In other words, `hstack` can be visualized as two matrices with the same number of columns stacked on top of one another. Second, we assume that the sub-routine `PCA` returns the orthonormal eigenvectors as rows. This assures that the eigenvectors are rows of a template direction matrix of a parallelotope. Third, the `Maximize` and `Minimize` sub-routines encapsulate the linear programming procedures required to compute the support points as discussed in Equation 3.1. Both sub-routines take the feasible region as the first parameter and the objective function as the second parameter. Finally, the subroutine `TransformBundle` is the same as specified in Algorithm 2.4.

Algorithm 3.1 computes the dynamic templates for each time step k . Line 7 computes the linear approximation of the non-linear dynamics and this linear approximation is used to compute the new


```

Input: Dynamics  $f$ , Initial Parallelotope  $P_0$ , Step Bound  $S$ , Lifespan Parameter  $L$ 
Output: Reachable Set Overapproximation  $\bar{\Theta}_k$  at each step  $k$ 
1  $Q_0 = \{P_0\}$ 
2  $\Lambda^{accum} = I_n$ 
3  $\Lambda^{Q_0} = \Lambda^{P_0}$  // Init Template Directions
4 for  $k \in [1, 2, \dots, S]$  do
5    $P_{supp} = \text{GetSupportPoints}(Q_{k-1})$  (support points of  $Q_{k-1}$ )
6    $P_{prop} = \text{PropagatePointsOneStep}(P_{supp}, f)$  (image of support points)
7    $A = \text{ApproxLinearTrans}(P_{supp}, P_{prop})$ 
8    $\Lambda^{accum} = \Lambda^{accum} \cdot A^{-1}$ 
9    $\Lambda_k^{lin} = \Lambda^{accum}$ 
10
11    $\Lambda_k^{pca} = \text{PCA}(P_{prop})$ 
12    $\Lambda_k = \text{hstack}(\Lambda_k^{lin}, \Lambda_k^{pca})$ 
13    $\Lambda^{total} = \Lambda_k$ 
14   for  $i \in [1, 2, \dots, L]$  do
15     // If  $L = 0$ , then skip
16      $\Lambda^{total} = \text{hstack}(\Lambda^{total}, \Lambda_{k-i})$ 
17   end
18
19    $Q_k = \text{TransformBundle}(f, Q_{k-1}, \Lambda_k)$ 
20    $\bar{\Theta}_k \leftarrow Q_k$ 
21 end
22 return  $\bar{\Theta}_1 \dots \bar{\Theta}_S$ 
23
24 Proc  $\text{GetSupportPoints}(Q)$  :
25    $P_{supp} = \emptyset$ 
26   for  $P \in \mathcal{P}(Q)$  do
27     for  $i \in [1, 2, \dots, n]$  do
28        $P_{supp} = P_{supp} \cup \text{Maximize}(Q, \Lambda_i^P) \cup \text{Maximize}(Q, -\Lambda_i^P)$ 
29     end
30   end
31   return  $P_{supp}$ 

```

Figure 3.1: The Automatic, Dynamic Reachability Algorithm

template directions according to this linear transformation in Line 10. The PCA directions of the images of support points is computed in line 11. For the time step k , the linear approximation and PCA templates direction matrices are given as Λ_k^{lin} and Λ_k^{pca} , respectively. To improve the accuracy of the reachable set, we compute the overapproximation of the reachable set with respect to not just the template directions at the current step, but with respect to other template directions for time steps that are within the template lifespan parameter L . Alternatively, we assign each parallelotope a

parameter L which dictates the number of steps we keep the parallelotope in the bundle after adding it in the current step.

CHAPTER 4

Evaluations

4.1 Kaa

We evaluate the efficacy of our dynamic parallelotope bundle strategies with our tool, *Kaa*. *Kaa* is written in Python and relies on several modules to perform reachable set computation.

Numpy: The *Numpy* module is used to do all matrix computations, such as matrix multiplication and matrix inversions. It is also used to efficiently solve systems of linear equations, especially those which arise from converting from half-space representation to generator representation (See Section 2.2.1), and execute the Least Squares routine required to compute the solution to Problem 3.2.

Sympy: The *Sympy* module is used to do all symbolic computations. The polynomials which result from performing the $\Lambda_i \cdot f(x)$ in Equation 2.30 are all simplified and encapsulated by the `sp.Poly` object. This allows extraction of coefficients of monomial terms to become a simple call to `sp.Poly.coeff_monomial`.

Sklearn: The *Sklearn* module called to perform PCA on the end-points of the sample trajectories as described in Section 3.2. The exact method is `sklearn.decomposition.PCA`.

Scipy: The *Scipy* module offers several auxiliary routines important to the our analysis of reachable sets, especially `scipy.spatial.ConvexHull`.

Matplotlib: The *Matplotlib* module is for all plotting of the computed reachable sets. *Kaa* utilizes the library's animation features to even animate the evolution of the parallelotope bundle as the reachable set computation proceeds.

Multiprocessing: The *multiprocessing* module parallelizes all the non-linear optimization procedures required to compute the new upper and lower offsets of all the template directions of the parallelotope bundle. This is expressed by lines 13,14 in Algorithm 2.4.

Swiglpk: The *swiglpk* module is a simple Python wrapper over the C library, *GLPK* (GNU Linear Programming Kit). Kaa uses *swiglpk* for all LP problems, such as those which arise from computing the support points over a bundle (see Equation 3.1).

The original version of Kaa was created to compactify and simplify *Sapo*, a previous tool exploring reachability computation with static parallelotope bundles (Dreossi, 2017). Through the expressiveness and terseness of Python, Algorithm 2.4 was implemented in only 650 lines of code. We released as a pedagogical tool to allow practitioners and students to easily experiment with parallelotopes-based reachability and understand the effects of choosing different template directions (Kim and Duggirala, 2020).

To extend Kaa to handle dynamic parallelotope bundles, we replaced the original optimization procedure leveraging Bernstein polynomials (see Section 2.2.2) to *Kodiak*. Kodiak is an optimization library implemented in C++ that implements a branch-and-bound algorithm for numerical approximations. It uses a combination of interval arithmetic and Bernstein enclosure to approximate solutions to optimization problems of the form shown in Equation 2.26. The optimization procedure for finding the direction offsets is performed through Kodiak. We decided to use Kodiak primarily for two reasons:

1. Kodiak is very fast as a Python wrapper over the original C++ implementation. It is much faster than Kaa’s original procedure of computing all Bernstein coefficients.
2. Kodiak can handle a wider variety of dynamics, including those which feature trigonometric terms and square root terms. This allows us to generalize beyond the polynomial dynamics first considered by (Dreossi et al., 2016).

To estimate volume of reachable sets, we employ two techniques for estimating the volume of individual parallelotope bundles. For systems of dimension fewer than or equal to three, we utilize Scipy’s convex hull routine, `scipy.spatial.ConvexHull`. For higher-dimensional systems, we employ the volume of the tightest enveloping box around the parallelotope bundle. The total volume estimate of the over-approximation

will be the sum of all the computed bundles' volume estimates. To be specific, if `ApproxVol` is the routine used to approximate the volume of a bundle, then by the notation introduced in line 22 of Algorithm ??:

$$\text{ApproxVol}(\bar{\Theta}) = \sum_k \text{ApproxVol}(\bar{\Theta}_k) \quad (4.1)$$

4.2 Benchmarks

For benchmarking, we select six non-linear models with polynomial dynamics. Since many of these models are also implemented in Sapo, we choose benchmarks with polynomial dynamics to directly compare the performance of our dynamic strategies with the Sapo's static parallelotopes. To provide meaningful comparisons, we set the number of dynamic parallelotopes to be equal to the number of static ones excluding the initial box. Recall through the discussion in Example 2.3 that we refer to parallelotopes defined only by axis-aligned and diagonal directions as *diagonal parallelotopes*. Similarly, *diagonal parallelotope bundles* are parallelotope bundles solely consisting of diagonal parallelotopes. Sapo primarily utilizes *static diagonal parallelotope bundles* to perform its reachability computation. Note that the initial box, which is defined only through the axis-aligned directions, is contained in every bundle. For our experiments, we are concerned with the effects of additional static or dynamic parallelotopes added alongside the initial box. We refer to these parallelotopes *non-axis-aligned parallelotopes*.

Table 4.1 summarizes five standard benchmarks used for experimentation. The last seven-dimensional COVID supermodel is explained in the subsequent section below.

4.3 COVID19 Supermodel

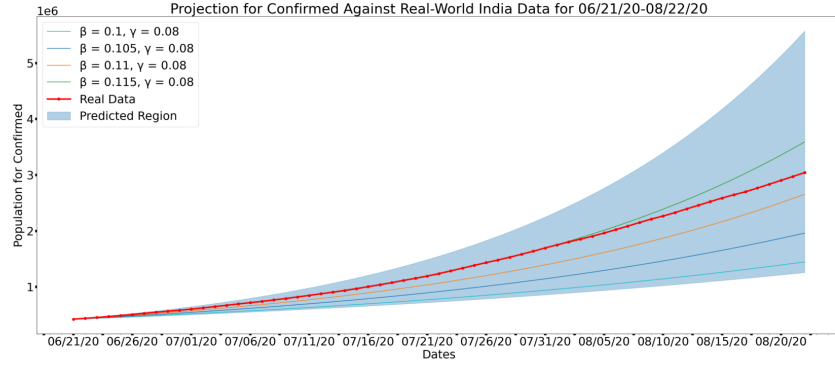
We benchmark our dynamic strategies with the recently introduced COVID supermodel (Ansumali et al., 2020), (National Supermodel Committee , 2020). This model is a modified SIR model accounting for the possibility of *asymptomatic* patients. These patients can infect susceptible members with a fixed probability. The dynamics account for this new group and its interactions with the traditional SIR groups.

$$\begin{aligned}
S'_A &= S_A - (\beta S_A(A + I)) \cdot \Delta \\
S'_I &= S_I - (\beta S_I(A + I)) \cdot \Delta \\
A' &= A + (\beta S_I(A + I) - \gamma I) \cdot \Delta \\
I' &= I + (\beta S_I(A + I) - \gamma I) \cdot \Delta \\
R'_A &= R_A + (\gamma A) \cdot \Delta \\
R'_I &= R_I + (\gamma I) \cdot \Delta \\
D' &= D + (\eta I) \cdot \Delta
\end{aligned}$$

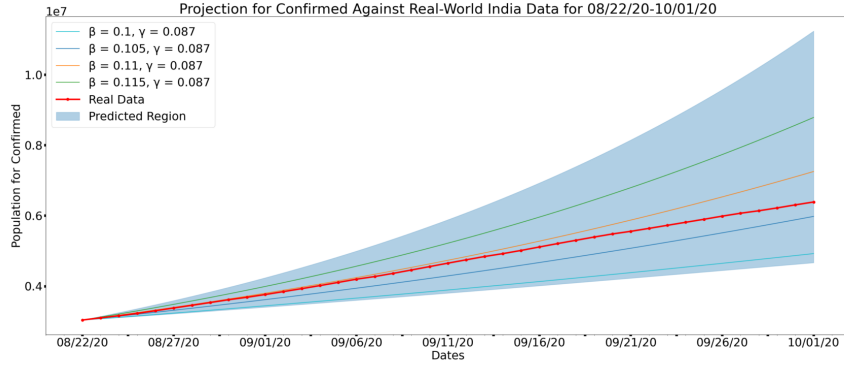
Figure 4.1: Dynamics for the COVID19 Supermodel.

where the variables denote the fraction of a population of individuals designated as *Susceptible to Asymptomatic* (S_A), *Susceptible to Symptomatic* (S_I), *Asymptomatic* (A), *Symptomatic* (I), *Removed from Asymptomatic* (R_A), *Removed from Symptomatic* (R_I), and *Deceased* (D). We choose the parameters ($\beta = 0.25, \gamma = 0.02, \eta = 0.02$) where β is the probability of infection, γ is the removal rate, and η is the mortality rate. The parameters are set based on figures shown in (Ansumali et al., 2020). The discretization step is chosen to be $\Delta = 0.1$ and the initial box is set to be following dimensions: $S_A \in [0.69, 0.7]$, $S_I \in [0.09, 0.1]$, $A \in [0.14, 0.15]$, $I \in [0.04, 0.05]$, $R_A = 0$, $R_I = 0$, $D = 0$. The discretized dynamics are given in Figure 4.1.

Plots of the reachable set for this model tuned to specific values of parameters β, γ, η were published in an ACM Sigbed Blogpost detailing applications of Formal methods for simulating disease dynamics (Bak et al., 2021b). The main theme of the blogpost revolved around the difficulty of extracting accurate parameters from real-world data samples. Certainly we can estimate the parameters by analyzing real-world data. However, minute changes in the parameters could yield estimates which would vastly overestimate or underestimate the true population of infected or asymptomatic patients. This error is further compounded as our time horizon increases due to many of the issues pertaining to wrapping error, as discussed in the Introduction of this thesis (see Section 1). Reachability analysis provides not only a method of simulating the disease dynamics in order to provide illuminating information for policy decisions but also to demonstrate the effect of slight



(a) Confirmed population from 06/21/20-08/22/20,



(b) Confirmed population from 08/22/20-10/01/20

Figure 4.2: Reachable Sets for India's COVID19 Confirmed Population for the period 06/21/20-10/01/20

changes in the parameters on the conservativeness of the outputted reachable set. See Figure 4.2 for the two plots published in the blogpost. The Confirmed population is the sum of the number of Symptomatic (I) and Asymptomatic (A) populations of the dynamics presented in Equation ???. The plots were created by dividing the total period into two separate periods. We decided to separate the periods as the parameters presented in the original paper (Ansumali et al., 2020) were estimated separately according to these exact periods. Furthermore, we wished to control the conservativeness of the over-approximation of the reachable set. The red line represents the real data gathered from India during the prescribed time periods with the light-blue region representing the predicted region based on the parameters given in (Ansumali et al., 2020). Several lines representing trajectories generated according to specific parameters are also plotted in order to convey the effect of changes in the population under slight perturbations of the underlying parameters.

Model	Dimension	Parameters	# steps	Δ	Initial Box
Vanderpol	2	–	70	0.08	$x \in [0, 0.1]$ $y \in [1.99, 2]$
Jet Engine	2	–	100	0.2	$x \in [0.8, 1.2]$ $y \in [0, 8, 1.2]$
Neuron	2	–	200	0.2	$x \in [0.9, 1.1]$ $y \in [2.4, 2.6]$
SIR	3	$\beta = 0.05$ $\gamma = 0.34$	150	0.1	$s \in [0.79, 0.8]$ $i \in [0.19, 0.2]$ $r = 0$
Coupled Vanderpol	4	–	40	0.08	$x_1 \in [1.25, 2.25]$ $y_1 \in [1.25, 2.25]$ $x_2 \in [1.25, 2.25]$ $y_2 \in [1.25, 2.25]$
COVID	7	$\beta = 0.05$ $\gamma = 0.0$ $\eta = 0.02$	200	0.08	Stated in Section 4.3

Table 4.1: Benchmark models and relevant information

4.4 Comparison of Template Generation Techniques

4.4.1 Accuracy of Dynamic Strategies

The results of testing our dynamic strategies against static ones are summarized in Table 4.4. For models previously defined in Sapo, we set the static parallelotopes to be exactly those found in Sapo. If a model is not implemented in Sapo, we simply use the static parallelotopes defined in a model of equal dimension. To address the unavailability of a four-dimensional model implemented in Sapo, we sampled random subsets of five static non-axis-aligned parallelotopes and chose the flowpipe with smallest volume. A cursory analysis shows that the number of possible templates with diagonal directions grows with $O(n^n)$ with the number of dimensions and hence an exhaustive search on optimal template directions is infeasible.

From our experiments, we conclude there is no universal optimal ratio between the number of dynamic parallelotopes defined by PCA and Linear Approximation directions which perform well on all benchmarks. In Figure 4.3, we demonstrate two cases where varying the ratio imparts differing effects. Observe that using parallelotopes defined by linear approximation directions is

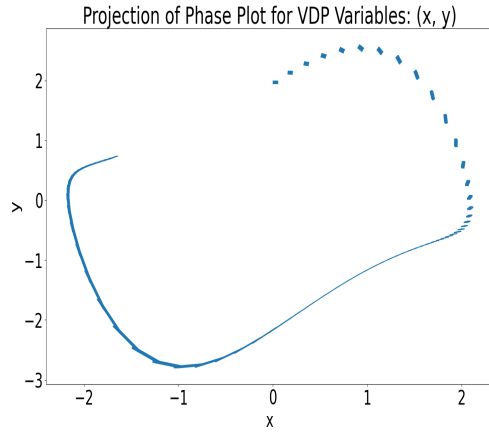
more effective than those defined by PCA directions in the Vanderpol model whereas the Neuron model shows the opposite trend.

4.4.2 Performance under Increasing Initial Sets

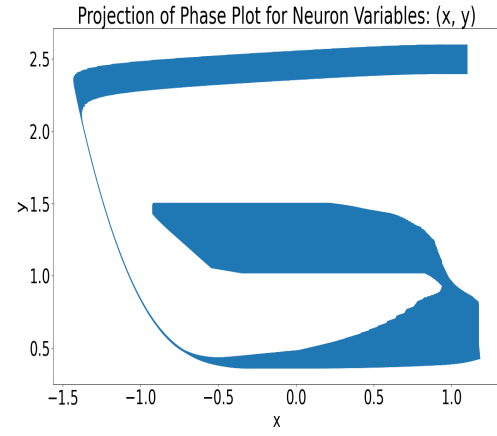
A key advantage of our dynamic strategies is the improved ability to control the wrapping error naturally arising from larger initial sets. Figure 4.5 presents charts showcasing the effect of increasing initial sets on the total flowpipe volume. We vary the initial box dimensions to gradually increase the box’s volume. We then plot the total flowpipe volume after running the benchmark. The same initial boxes are also used in computations using Sapo’s static parallelotopes. The number of parallelotopes defined by PCA and Linear Approximation directions were chosen based on best performance as seen in Table 4.4. We remark that our dynamic strategies perform better than static ones in controlling the total flowpipe volume as the initial set becomes larger. On the other hand, the performance of static parallelotopes tends to degrade rapidly as we increase the volume of the initial box.

4.4.3 Performance against Random Static Templates

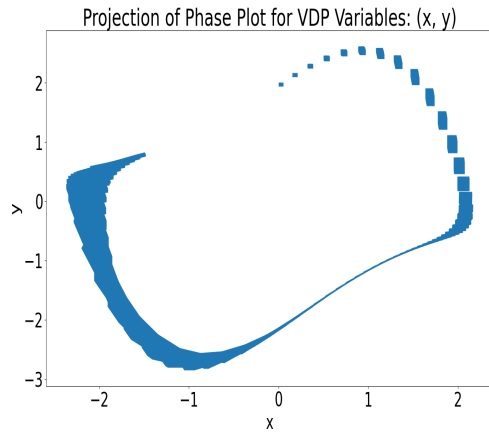
We additionally benchmark our dynamic strategies against static random parallelotope bundles. We sample such parallelotopes in n dimensions by first sampling a set of n directions uniformly on the surface of the unit $(n - 1)$ -sphere, then defining our parallelotope using these sampled directions. We sample twenty of these parallelotopes for each trial and average the total flowpipe volumes. As shown in Figure 4.6, our best-performing dynamic strategies consistently outperform static random strategies for all tested benchmarks.



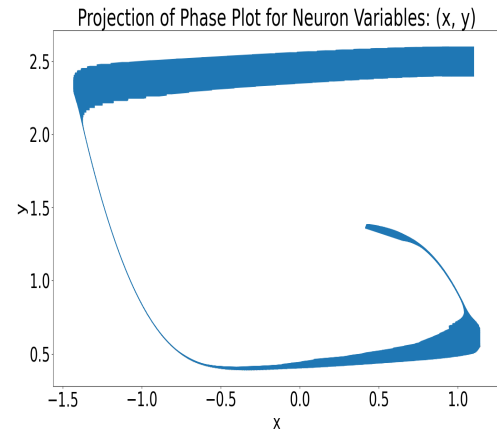
(a) 5 Lin



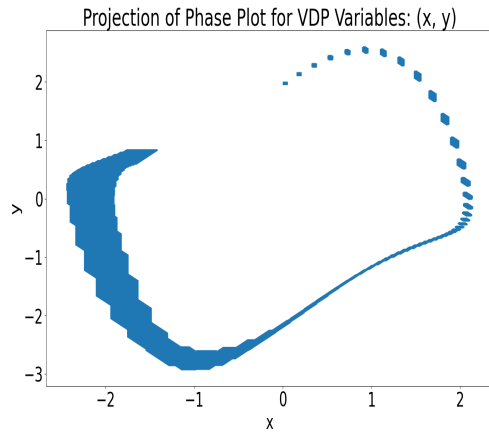
(b) 1 PCA 5 Lin



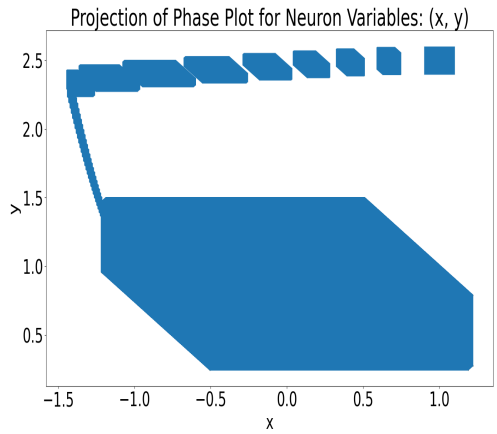
(c) 5 PCA



(d) 5 PCA 1 Lin



(e) Sapo



(f) Sapo

Figure 4.3: Effect of varying ratio between the number of PCA and Linear Approximation parallelotopes. The Vanderpol (left) and the FitzHugh-Nagumo Neuron (right) phase plots are shown to illustrate differing effects of varying the PCA/LinApp ratio. The initial set for the Vanderpol model is set to $x \in [0, 0.05]$, $y \in [1.95, 2]$, and the initial set Neuron model is set to $x \in [0.9, 1.1]$, $y \in [2.4, 2.6]$

Strategy	Total Volume
5 LinApp	0.227911
1 PCA, 4 LinApp	0.225917
2 PCA, 3 LinApp	0.195573
3 PCA, 2 LinApp	0.188873
4 PCA, 1 LinApp	1.227753
5 PCA	1.509897
5 Static Diagonal(Sapo)	2.863307

(a) Vanderpol

Strategy	Total Volume
5 LinApp	58199.62
1 PCA, 4 LinApp	31486.16
2 PCA, 3 LinApp	5204.09
3 PCA, 2 LinApp	6681.76
4 PCA, 1 LinApp	50505.10
5 PCA	84191.15
5 Static Diagonal (Sapo)	66182.18

(b) Jet Engine

Strategy	Total Volume
5 LinApp	154.078
1 PCA, 4 LinApp	136.089
2 PCA, 3 LinApp	73.420
3 PCA, 2 LinApp	73.126
4 PCA, 1 LinApp	76.33
5 PCA	83.896
5 Static Diagonal (Sapo)	202.406

(c) FitzHugh-Nagumo

Strategy	Total Volume
2 LinApp	0.001423
1 PCA, 1 LinApp	0.106546
2 PCA	0.117347
2 Static Diagonal (Sapo)	0.020894

(d) SIR

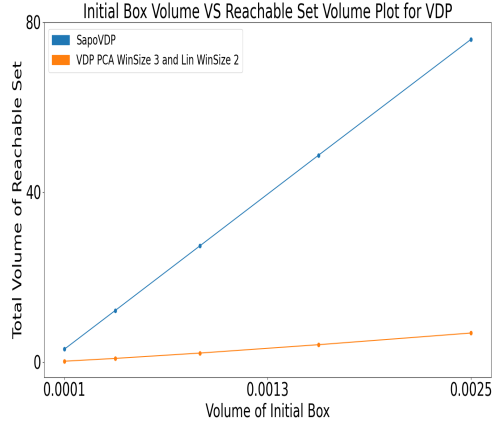
Strategy	Total Volume
5 LinApp	5.5171
1 PCA, 4 LinApp	5.2536
2 PCA, 3 LinApp	5.6670
3 PCA, 2 LinApp	5.5824
4 PCA, 1 LinApp	312.2108
5 PCA	388.0513
5 Static Diagonal (Best)	3023.4463

(e) Coupled Vanderpol

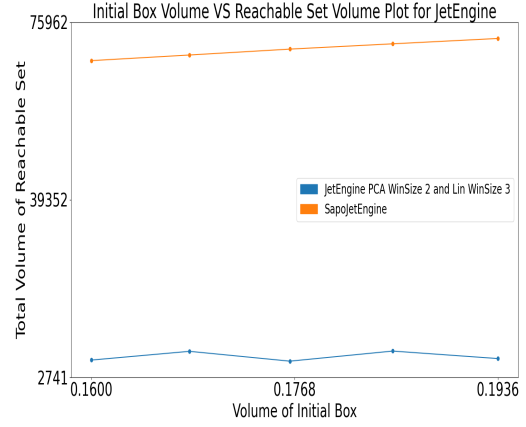
Strategy	Total Volume
3 LinApp	$2.95582227 * 10^{-10}$
1 PCA, 2 LinApp	$2.33007583 * 10^{-10}$
2 PCA, 1 LinApp	$4.02751770 * 10^{-9}$
3 PCA	$4.02749571 * 10^{-9}$
3 Static Diagonal (Sapo)	$4.02749571 * 10^{-9}$

(f) COVID

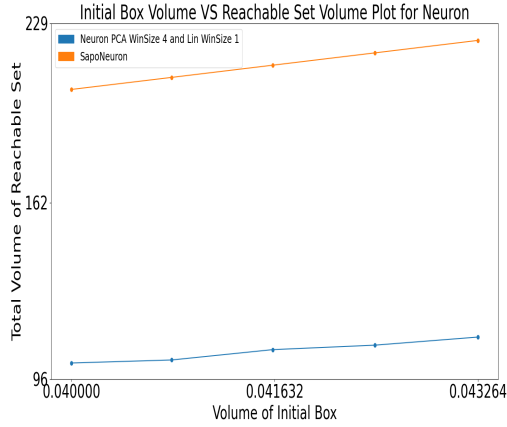
Figure 4.4: Tables presenting upper bounds on the total reachable set volume by strategy. The static directions are retrieved and/or inspired from Sapo models of equal dimension for benchmarking. The best performing strategy is highlighted in bold.



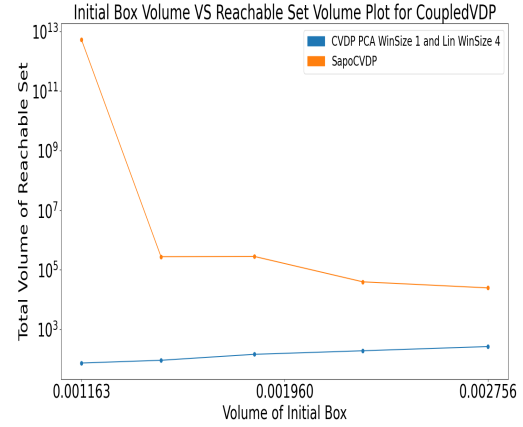
(a) Vanderpol



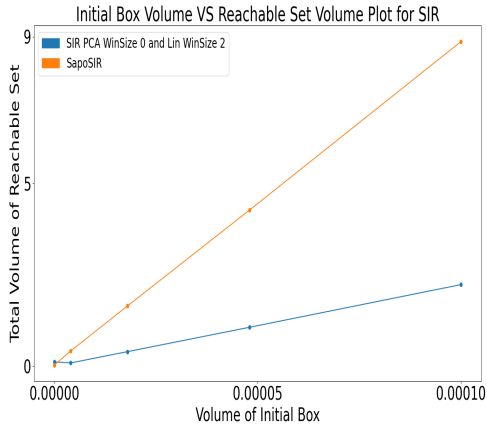
(b) Jet Engine



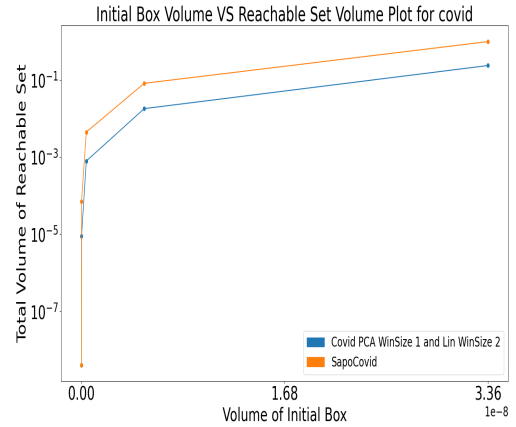
(c) Neuron



(d) Coupled Vanderpol

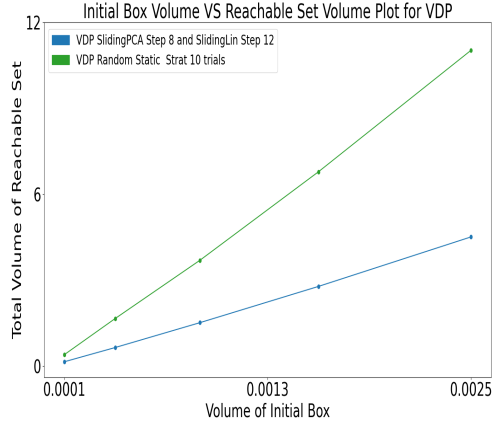


(e) SIR

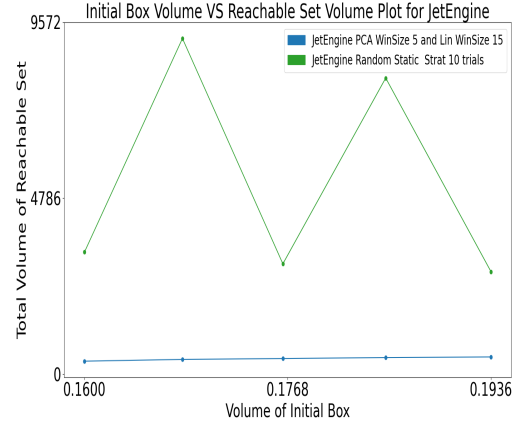


(f) COVID

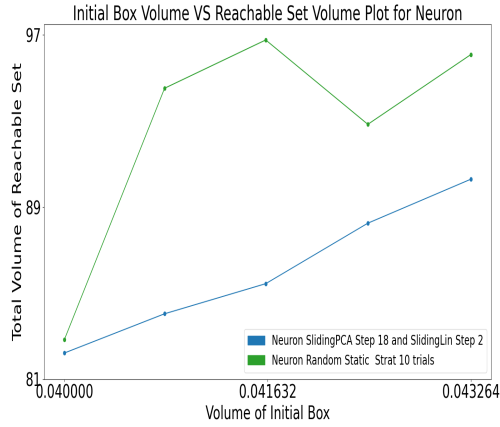
Figure 4.5: Comparison between the performance of diagonal static parallelotope bundles and that of the best performing dynamic parallelotope bundles as the volume of the initial set grows.



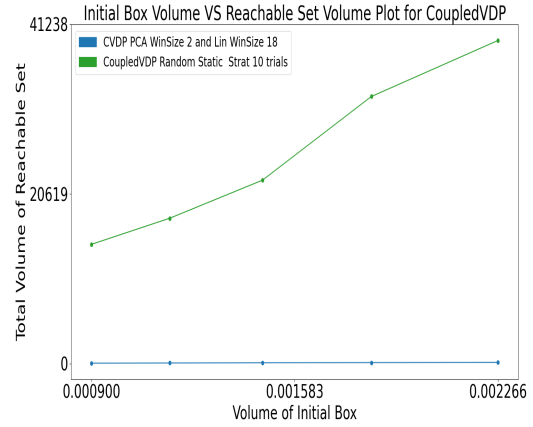
(a) Vanderpol



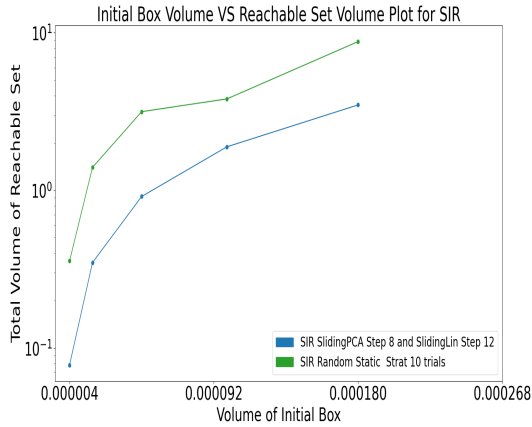
(b) Jet Engine



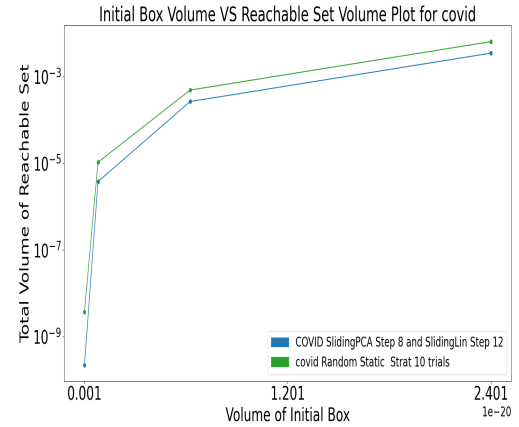
(c) Neuron



(d) Coupled Vanderpol



(e) SIR



(f) COVID

Figure 4.6: Comparison between random static strategies and the best performing dynamic strategies as the volume of the initial set grows. The total reachable set volumes for random static strategies are averaged over ten trials for each system.

S

CHAPTER 5

Conclusion

In this paper, we investigated two techniques for generating templates dynamically: first using linear approximation of the dynamics, and second using PCA. We demonstrated that these techniques improve the accuracy of reachable set by an order of magnitude when compared to static or random template directions. We also observed that both these techniques improve the accuracy of the reachable sets for different benchmarks. In future, we intend to investigate Koopman linearization techniques for computing alternative linear approximation template directions (Bak et al., 2021a). We also wish to investigate the use of a massively-parallel implementation using HPC hardware such as GPUs for optimizing over an extremely large number of parallelotopes and their template directions. This is inspired by the approach behind the recent tool *PIRK* (Devonport et al., 2020).

BIBLIOGRAPHY

- Althoff, M. (2010). *Reachability analysis and its application to the safety assessment of autonomous cars*. PhD thesis, Technische Universität München.
- Althoff, M., Stursberg, O., and Buss, M. (2010). Computing reachable sets of hybrid systems using a combination of zonotopes and polytopes. *Nonlinear analysis: hybrid systems*, 4(2):233–249.
- Ansumali, S., Kaushal, S., Kumar, A., Prakash, M. K., and Vidyasagar, M. (2020). Modelling a pandemic with asymptomatic patients, impact of lockdown and herd immunity, with applications to sars-cov-2. *Annual Reviews in Control*.
- Bak, S. (2021). nnenum: Verification of relu neural networks with optimized abstraction refinement. In *NASA Formal Methods Symposium*, pages 19–36. Springer.
- Bak, S., Bogomolov, S., Duggirala, P. S., Gerlach, A. R., and Potomkin, K. (2021a). Reachability of black-box nonlinear systems after Koopman operator linearization.
- Bak, S. and Duggirala, P. S. (2017). Simulation-equivalent reachability of large linear systems with inputs. In *International Conference on Computer Aided Verification*, pages 401–420. Springer.
- Bak, S., Kim, E., and Duggirala, P. S. (2021b). Covid infection prediction using cps formal verification methods.
- Boyd, S., Boyd, S. P., and Vandenberghe, L. (2004). *Convex optimization*. Cambridge university press.
- Chen, X. and Ábrahám, E. (2011). Choice of directions for the approximation of reachable sets for hybrid systems. In *International Conference on Computer Aided Systems Theory*, pages 535–542. Springer.
- Clarisó, R. and Cortadella, J. (2004). The octahedron abstract domain. In *International Static Analysis Symposium*, pages 312–327. Springer.
- Dang, T., Dreossi, T., and Piazza, C. (2014). Parameter synthesis using parallelotopic enclosure and applications to epidemic models. In *International Workshop on Hybrid Systems Biology*, pages 67–82. Springer.
- Dang, T. and Gawlitza, T. M. (2011). Template-based unbounded time verification of affine hybrid automata. In *Asian Symposium on Programming Languages and Systems*, pages 34–49. Springer.
- Dang, T. and Maler, O. (1998). Reachability analysis via face lifting. In *International Workshop on Hybrid Systems: Computation and Control*, pages 96–109. Springer.
- Dang, T. and Salinas, D. (2009). Image computation for polynomial dynamical systems using the Bernstein expansion. In *International Conference on Computer Aided Verification*, pages 219–232. Springer.
- Dang, T. and Testylier, R. (2012). Reachability analysis for polynomial dynamical systems using the Bernstein expansion. *Reliable Computing*, 17(2):128–152.

- Devonport, A., Khaled, M., Arcak, M., and Zamani, M. (2020). PIRK: Scalable interval reachability analysis for high-dimensional nonlinear systems. In *International Conference on Computer Aided Verification*, pages 556–568. Springer.
- Dreossi, T. (2017). Sapo: Reachability computation and parameter synthesis of polynomial dynamical systems. In *Proceedings of the 20th International Conference on Hybrid Systems: Computation and Control*, pages 29–34.
- Dreossi, T., Dang, T., and Piazza, C. (2016). Parallelotope bundles for polynomial reachability. In *Proceedings of the 19th International Conference on Hybrid Systems: Computation and Control*, pages 297–306.
- Dreossi, T., Dang, T., and Piazza, C. (2017). Reachability computation for polynomial dynamical systems. *Formal Methods in System Design*, 50(1):1–38.
- Duggirala, P. S. and Viswanathan, M. (2016). Parsimonious, simulation based verification of linear systems. In *International Conference on Computer Aided Verification*, pages 477–494. Springer.
- Fan, J., Huang, C., Chen, X., Li, W., and Zhu, Q. (2020). Reachnn*: A tool for reachability analysis of neural-network controlled systems. In *International Symposium on Automated Technology for Verification and Analysis*, pages 537–542. Springer.
- FitzHugh, R. (1961). Impulses and physiological states in theoretical models of nerve membrane. *Biophysical journal*, 1(6):445–466.
- Garloff, J. (2003). The Bernstein expansion and its applications. *Journal of the American Romanian Academy*, 25:27.
- Geretti, L., Althoff, M., Benet, L., Chapoutot, A., Collins, P., Duggirala, P. S., Forets, M., Kim, E., Linares, U., et al. (2021). Arch-comp21 category report: Continuous and hybrid systems with nonlinear dynamics.
- Girard, A. (2005). Reachability of uncertain linear systems using zonotopes. In *International Workshop on Hybrid Systems: Computation and Control*, pages 291–305. Springer.
- Gronski, J., Sassi, M.-A. B., Becker, S., and Sankaranarayanan, S. (2019). Template polyhedra and bilinear optimization. *Formal Methods in System Design*, 54(1):27–63.
- Heidlauf, P., Collins, A., Bolender, M., and Bak, S. (2018). Verification challenges in f-16 ground collision avoidance and other automated maneuvers. In *ARCH@ ADHS*, pages 208–217.
- Kim, E., Bak, S., and Duggirala, P. S. (2021). Automatic dynamic parallelotope bundles for reachability analysis of nonlinear systems. In *International Conference on Formal Modeling and Analysis of Timed Systems*, pages 50–66. Springer.
- Kim, E. and Duggirala, P. S. (2020). Kaa: A Python implementation of reachable set computation using Bernstein polynomials. *EPiC Series in Computing*, 74:184–196.
- Muñoz, C. and Narkawicz, A. (2013). Formalization of Bernstein polynomials and applications to global optimization. *Journal of Automated Reasoning*, 51(2):151–196.
- Nataraj, P. S. and Arounassalame, M. (2007). A new subdivision algorithm for the Bernstein polynomial approach to global optimization. *International journal of automation and computing*, 4(4):342–352.

- Nataray, P. and Kotecha, K. (2002). An algorithm for global optimization using the Taylor–Bernstein form as inclusion function. *Journal of Global Optimization*, 24(4):417–436.
- National Supermodel Committee (2020). Indian Supermodel for Covid-19 Pandemic.
- Sankaranarayanan, S., Dang, T., and Ivančić, F. (2008). Symbolic model checking of hybrid systems using template polyhedra. In *International Conference on Tools and Algorithms for the Construction and Analysis of Systems*, pages 188–202. Springer.
- Sassi, M. A. B., Testylier, R., Dang, T., and Girard, A. (2012). Reachability analysis of polynomial systems using linear programming relaxations. In *International Symposium on Automated Technology for Verification and Analysis*, pages 137–151. Springer.
- Seladji, Y. (2017). Finding relevant templates via the principal component analysis. In *International Conference on Verification, Model Checking, and Abstract Interpretation*, pages 483–499. Springer.
- Smith, A. P. (2009). Fast construction of constant bound functions for sparse polynomials. *Journal of Global Optimization*, 43(2-3):445–458.
- Stursberg, O. and Krogh, B. H. (2003). Efficient representation and computation of reachable sets for hybrid systems. In *International Workshop on Hybrid Systems: Computation and Control*, pages 482–497. Springer.
- Tran, H.-D., Manzananas Lopez, D., Musau, P., Yang, X., Nguyen, L. V., Xiang, W., and Johnson, T. T. (2019). Star-based reachability analysis of deep neural networks. In *International symposium on formal methods*, pages 670–686. Springer.
- Wangersky, P. J. (1978). Lotka-volterra population models. *Annual Review of Ecology and Systematics*, 9:189–218.